Received: 20 June 2022 | Revised: 15 February 2023 | Accepted: 7 March 2023

DOI: 10.1002/ppp.2187

WILEY

RESEARCH ARTICLE

Sensitivity of simulated frozen ground temperatures to different solar radiation and air temperature products—a case study in the Qilian Mountains in West China

Yanlin Zhang[1] | Xin Li[2] | Xiaoli Chang[1,3] | Huijun Jin[3,4] | Anning Huang[5] | Ji Liang[1] | Guodong Cheng[2,4,6] | Xin Wang[1]

[1]School of Earth Sciences and Spatial Information Engineering, Hunan University of Science and Technology, Xiangtan, Hunnan Province, China

[2]CAS Centre for Excellence in Tibetan Plateau Earth Sciences, Chinese Academy of Sciences, Beijing, China

[3]School of Civil Engineering, Institute of Cold-Regions Engineering Science and Technology, and Northeast-China Observatory and Research-Station of Permafrost Geo-Environment-Ministry of Education, Northeast Forestry University, Harbin, China

[4]Da-Xing'anling Observatory and Research Station of Permafrost Engineering and Environment and State Key Laboratory of Frozen Soils Engineering, Northwest Institute of Eco-Environment and Resources, Chinese Academy of Sciences, Lanzhou, China

[5]CMA-NJU Joint Laboratory for Climate Prediction Studies, State Key Laboratory of Severe Weather and Joint Center for Atmospheric Radar Research of CMA/NJU, School of Atmospheric Sciences, Nanjing University, Nanjing, China

[6]Institute of Urban Study, Shanghai Normal University, Shanghai, China

Correspondence
Xiaoli Chang, School of Civil Engineering, Institute of Cold-Regions Engineering Science and Technology, and Northeast-China Observatory and Research-Station of Permafrost Geo-Environment-Ministry of Education, Northeast Forestry University, Harbin, China.
Email: changxiaoli2002@163.com

Funding information
National Natural Science Foundation of China, Grant/Award Numbers: 41975081, 41671059, 41971079; Strategic Priority Research Program of the Chinese Academy of Sciences, Grant/Award Number: XDA20100103

Abstract

Downward solar radiation (DSR) and air temperature (Ta) have significant influences on the thermal state of frozen ground. These parameters are also important forcing terms for physically based land surface models (LSMs). However, the quantitative influences of inaccuracies in DSR and Ta products on simulated frozen ground temperatures remain unclear. In this study, three DSR products (CMFD-SR, Tang-SR, and GLDAS-SR) and two Ta products (CMFD-Ta and GLDAS-Ta) were used to force an LSM model in an alpine watershed in Northwest China, to investigate the sensitivity of simulated ground temperatures to different DSR and Ta products. Compared to a control model (CTRL) forced by *in situ* observed DSR, ground temperatures simulated by the experimental model forced by GLDAS-SR are obviously decreased because GLDAS-SR is much lower than *in situ* observations. Instead, simulation results in models forced by CMFD-SR and Tang-SR are much closer to those of CTRL. Ta products led to significant errors in simulated ground temperatures. In conclusion, both CMFD-SR and Tang-SR could be used as good alternatives to *in situ* observed DSR for forcing a model, with acceptable errors in simulation results. However, more care need to be paid for models forced by Ta products instead of Ta observations, and conclusions should be carefully drawn.

KEYWORDS
frozen ground, ground temperature, land surface model, meteorological forcing, solar radiation

1 | INTRODUCTION

The spatial distribution and thermal dynamics of frozen ground (including permafrost and seasonal frost) have attracted extensive attention worldwide,[1–5] because they could have significant impacts on terrestrial eco-hydrological processes[6–10] and carbon cycling through modulating soil thermal–hydraulic properties and the decomposition rate of organic matter.[11–13] The thermal state of frozen ground is regulated by the surface energy balance, which is jointly controlled by climatic conditions, such as solar radiation and air temperature, and local factors, including topography, snow cover, vegetation condition, moisture, among others.[14–19]

Solar radiation and air temperature are crucial to the energy exchange between the ground and atmosphere, and they are key variables for estimating the thermal state of frozen ground.[20,21] Solar radiation could become a dominating factor for permafrost mapping at a local or landscape scale in mountainous areas.[22,23] In recent decades, as a quantitative analysis tool for simulating heat and water transfer in the soil–vegetation–atmosphere system, physically based land surface models (LSMs)[24,25] have been widely used for mapping permafrost, predicting the responses of frozen ground to climate change,[26,27] and assessing their environmental consequences.[28] Solar radiation and air temperature are important forcing terms for LSMs, and accurate inputs are essential to achieving good simulation results for evapotranspiration, snowpack, ground temperatures, and moisture.[29–31] Distributed simulations at larger scales (e.g., continental or regional) require obtaining accurate datasets of spatial–temporally distributed air temperature (Ta) and downward solar radiation (DSR), which is a challenge with sparse *in situ* observations, especially in mountainous areas, where the impacts of terrain cannot be ignored.[32–35] In general, Ta and DSR have very strong spatial heterogeneities.[36,37] For example, at a given region and time, DSR depends on the atmospheric conditions (including water vapor content, cloud amount and thickness, and aerosol types and concentrations), and randomly floating clouds will reduce the DSR to varying degrees depending on the cloud amount and thickness.[38,39] However, in the long term, both DSR and Ta may display some horizontal and vertical zonalities under specific atmospheric circulation and climatic conditions.[37]

There are three main approaches often used to obtain a regionally distributed DSR and Ta, including spatial interpolation, output of global circulation models (GCMs) and its reanalysis, and remote sensing inversion technology. With a sparse and uneven network of observational stations mostly installed in easily accessible areas, spatial interpolation cannot effectively capture the spatial heterogeneity of DSR and Ta caused by some random factors, and therefore it will inevitably lead to large errors at locations far from the observational stations, especially for remote and alpine regions.[40,41] Although typically characterized by coarse spatial resolution and poor accuracy, some DSR and Ta products generated by GCMs and reanalysis technology, such as NCEP-1 (National Centers for Environmental Prediction Reanalysis 1), ERA-Interim (European Center for Medium-Range Weather Forecasts Reanalysis-Interim), JRA-55 (Japanese 55-year Reanalysis), MERRA (Modern-Era Retrospective analysis for Research and Applications), and GLDAS (Global Land Data Assimilation System), have been widely used for forcing LSMs at regional to continental scales.[42–44]

Estimating DSR based on remote sensing datasets and algorithms can be traced back to the 1980s.[45] In recent decades, with the increasing availability of remote sensors, many empirical methods,[46] and physically based models and algorithms making use of radiation transfer model and look-up tables[47,48] have been developed to retrieve DSR from remotely sensed products of clouds, vapor water content, and aerosols. Various global DSR products have been successively released, for example Global Energy and Water Exchanges Surface Radiation Budget (GEWEX-SRB),[49] International Satellite Cloud Climatology Project-FD-SRF,[50] Clouds and the Earth's Radiant Energy System Project-Energy Balanced and Filled,[51] and University of Maryland's surface radiation budget,[52] among others. Most of these products have a coarse spatial resolution and a poor accuracy in alpine regions in West China because of insufficient incorporation of local observations.[53,54] Various downscaling technology or remote sensing datasets of high spatial resolution have been used together with *in situ* observations to improve the local DSR. Yang et al[55] produced and validated a 3-hourly and 0.1° DSR dataset in China on the basis of GEWEX-SRB, and this is included in the China Meteorological Forcing Dataset (CMFD, and the DSR product is referred to as CMFD-SR hereafter). Based on the International Satellite Cloud Climatology Project (ISCCP) H-series pixel level gridded cloud products (HXG) and the European Center for Medium-Range Weather Forecasts Reanalysis v5 (ERA5), Tang et al[56] produced a 16-year (2000–2015), high-resolution (3 hr, 10 km) global shortwave solar radiation dataset (Tang-SR hereafter) using an improved physical parameterization scheme. There have also been some attempts to retrieve information on surface air temperature based on remote sensed datasets.[57,58] However, only daily or monthly mean or maximum/minimum values can be retrieved, which is far from ideal for driving LSMs.

Inaccuracies and uncertainties are inevitable in all the above-mentioned products, and their quantitative influences on simulations of the thermal state of frozen ground remain unclear and need to be investigated. Therefore, three DSR products (CMFD-SR, Tang-SR, and GLDAS-SR) and two Ta products (CMFD-Ta and GLDAS-Ta) were selected and validated against *in situ* measurements, and used to force a simultaneous heat and water transfer model in a cold and arid mountainous watershed in the Qilian Mountain on the northeastern Qinghai–Tibet Plateau in Northwest China. After model evaluation, simulation results of some experimental models forced by each DSR and Ta product were compared with simulation results from a control model (CTRL) forced by *in situ* observed meteorological data to investigate the influences of different DSR and Ta products on simulating the thermal state of frozen ground in LSMs.

2 | STUDY AREA, DATA, AND MODEL SETUP

2.1 | Study area and datasets

In this study, numerical experiments and analyses were conducted in the eastern upstream basin (i.e., the Babao River basin) of Hei'he River in the Qilian Mountains on the northeastern margin of the Qinghai–Tibet Plateau in Northwest China (Figure 1). With the elevation ranging from 2,640 to 5,000 m asl (above sea level) in a catchment area of about 2,450 km^2, the Babao River basin has a rugged terrain with great contrasts between ridges and valleys. Annual precipitation in the basin ranges from 270 to 600 mm, and the dominant ecological community is alpine meadow. Due to the high elevations, mean annual air temperature is about +1.7°C at the basin outlet (2,640 m asl) and about −4.1°C over the entire basin. Seasonally frozen ground, permafrost, alpine cold desert, seasonal snow cover, and glaciers exist in the basin. In the basin, continuous permafrost is distributed in regions above 4,000 m, with the active layer thickness (ALT) <2.0 m. Isolated permafrost occurs sporadically in regions lower than 4,000 m,[59] with a lower limit of elevation at about 3,650 m for south-facing slopes and 3,400 for north-facing slopes in regions with rich organic matter in soil. On average, the ALT at an elevation of 3,700 m is about 4 m, but can decrease to 2 m in peat.[60]

In the Babao River basin, a comprehensive observational system has been installed and maintained from the beginning of the Watershed Allied Telemetry Experimental Research program (WATER)[61] and in the successive Hei'he Watershed Allied Telemetry Experimental Research program (HIWATER),[62] which provided substantial data support for the present study. For example, meteorological data, including precipitation, DSR, air temperature, relative humidity, wind direction and speed, and atmospheric pressure, at five ordinary automatic weather stations (namely, ARSF, ARNF, HCG, EB, and JYL, see Figure 1) and one superstation (namely, AR, with many more other observing systems and variables, see https://data.tpdc.ac.cn/zh-hans/data/88688751-90af-44e7-8f73-e4f1aeedde2a) were collected from August 16, 2013 to December 31, 2014.

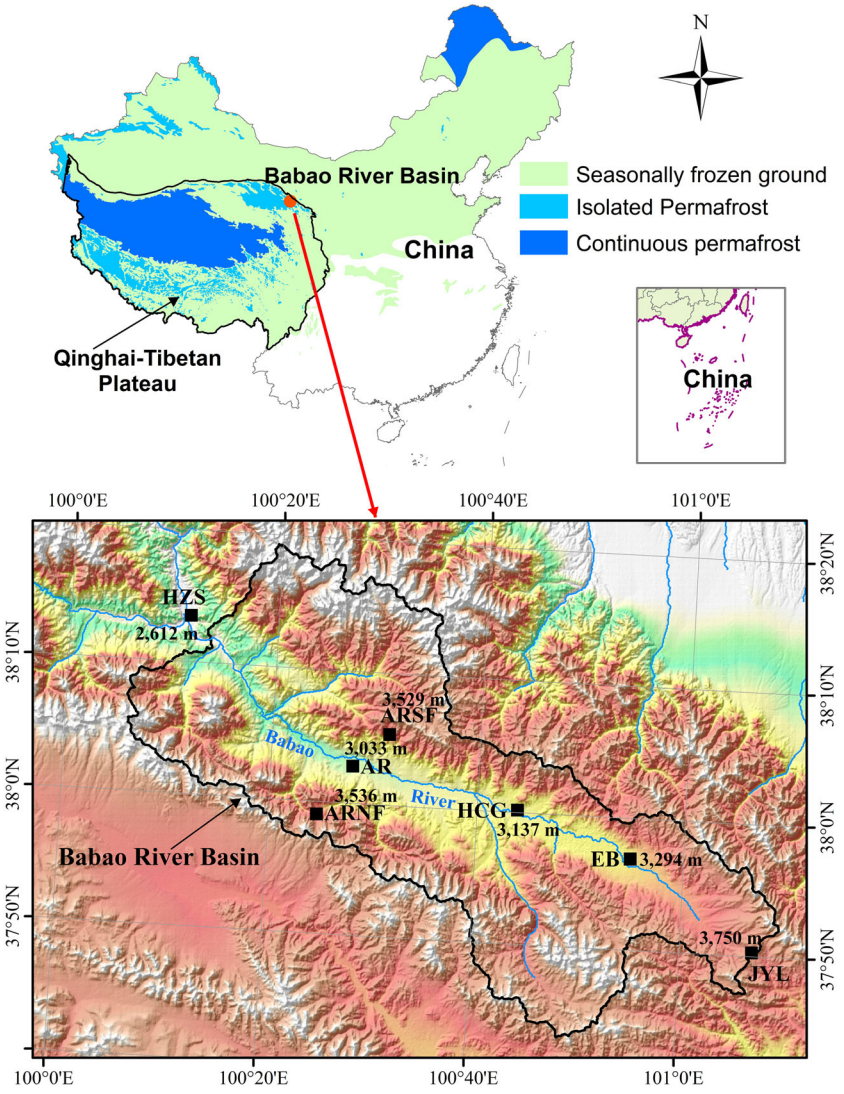

FIGURE 1 Topographical map of the Babao River basin. Automatic weather stations (AR, JYL, HCG, EB, ARNF, and ARSF) are indicated by black squares with elevations given. [Colour figure can be viewed at wileyonlinelibrary.com]

Sensors for monitoring ground temperature and volumetric soil water (liquid) content were installed at depths of 4, 10, 20, 40, 80, and 120 cm at all stations (including 160 and 240 cm at AR). In the entire observational period, all stations show unfrozen ground temperatures in summer or autumn at a depth of 1.2 m, which indicates the absence of permafrost or deep active layer. All stations except JYL, with elevations lower than 3,600 m (Figure 1), are located in areas of seasonally frozen ground. With an elevation of 3,750 m and rich organic matter in soil, station JYL is located in permafrost, with an ALT of about 3 m,[60] which is deeper than the observational domain. Meteorological data and ground temperatures recorded at 10-min temporal resolution were aggregated into hourly series. Hourly ground temperatures and volumetric soil water (liquid) content were used to assess model performance. These meteorological data can be downloaded from the National Tibetan Plateau/Third Pole Environment Data Center.[63] Land use and daily LAI (leaf area index) required by the model were from the datasets published by Ran et al[64] and Yuan et al,[65] respectively.

To investigate the influences of different DSR and Ta products on the simulated ground temperatures or thermal state, three DSR products (CMFD-SR, Tang-SR, and GLDAS-SR) and two Ta products (CMFD-Ta and GLDAS-Ta) were used to force an LSM in this study after validation against *in situ* measurements. All selected products have a 3-hourly time step. In validation, the 3-hourly series and their daily means were compared with the counterparts extracted or aggregated from hourly observations.

2.2 | Model setup and methods

An extended simultaneous heat and water transfer model (SHAW)[66,67] was used in this study. SHAW was initially designed for simulating the heat and water transfer in a vertical profile from either the top of the canopy, snow cover, or soil to a specified depth in the ground, which has been widely used in frozen ground analysis.[68] In the model, mutually coupled conservation equations for governing energy and water fluxes (see equations in Appendix A) were solved simultaneously using a finite difference method in a vertically layered system. Zhang et al[69] extended this into a spatially distributed framework (SHAWDHM) and implemented a mountainous solar radiation module with full consideration of slope orientation and topographic shadows in a complex terrain (algorithm details refer to Zhang et al[33]).

In this study, numerical modeling experiments were conducted at hourly time steps at six stations in the framework of SHAWDHM. Although five stations from six are located in seasonally frozen ground, the framework of this study is assumed to be used in a distributed way in the basin, where extensive permafrost exists. Therefore, the vertical model domain for the ground was set as confined from the soil surface to a constant depth of 15 m in the ground, to describe the future thermal and water transfer in permafrost. In the model, a self-adaptive layering system was used for canopy and snow stacking on the top of soil, according to the variation in canopy height (a growth curve was estimated for each vegetation type based on a few height observations in the year) and snow depth. The soil or ground was discretized into 15 horizontal layers, with calculating nodes fixed at 0.0, 0.04, 0.1, 0.2, 0.4, 0.8, 1.2, 1.6, 2.4, 4.0, 6.0, 9.0, 12.0, 14.0, and 15.0 m, respectively. To capture the large gradient and rapidly changing signal in ground temperature close to the surface, thin soil or ground layers were adopted. Layer thickness increased gradually downward, considering the compatibility of calculating nodes with station observation depths at the same time for the convenience of subsequent model validation. This discretization scheme of gradually increased layer thickness is often adopted in other LSMs.[25]

Soil parameters including bulk density, organic content, pore size distribution index, air entry potential, saturated hydraulic conductivity, porosity, field capacity, and soil texture were extracted from the dataset published by Dai et al[70] for depths from 0 to 2.4 m (the maximal depth for the dataset). Bulk density, porosity, and saturated conductivity were set to 1,600 kg/m^3, 0.1, and 10^{-8} m/s at depths below 2.4 m, and other parameters were set identical to those in the deepest layer in the dataset. A zero-flux condition was set for both heat and water transfer equations at the bottom boundary, and lateral heat and moisture exchanges were ignored. Initial model conditions, including snow depth, soil moisture content, and ground temperatures, were obtained through hundreds of spin-up cycles driven by 1-year meteorological data from August 16, 2013 to August 15, 2014 with arbitrarily given values at the beginning. Obtained initial ground temperatures and volumetric soil water (liquid) content profiles at all stations were validated against *in situ* observations (shown in Supporting Information Figures S1 and S2).

After evaluating the ground temperatures simulated by the control model (CTRL; see Table 1) forced by *in situ* observed meteorological data, sensitive experimental models were set up identical to CTRL except that either the input DSR or Ta was replaced by products in the model (e.g., CMFD-SR-Exp, Tang-SR-Exp, and others; see Table 1). The simulation results of all these experimental models were compared with CTRL to distinguish the influences of substitution of observed DSR or Ta by products on the simulated ground temperatures. For comparison, some experimental models (CMFD-Rh-Exp, CMFD-Wind-Exp, and others; see Table 1) centering on the influences of relative humidity (Rh) and wind speed (Wind) products were also set up identical to CTRL, except substituting the observed Rh and Wind in CTRL with products. All detailed descriptions of these experimental models are listed in Table 1.

To evaluate the accuracies of simulated ground temperatures and products of Ta or DSR, root mean squared error (RMSE) and bias (BIA) were selected as quantitative assessing criteria, as follows,

$$\mathrm{RMSE} = \sqrt{\sum_{i=1}^{N} (y_{si} - y_{oi})^2 / N}, \quad (1)$$

$$\mathrm{BIA} = \sum_{i=1}^{N} (y_{si} - y_{oi}) / N, \quad (2)$$

where y_{oi} is the observed or control series, y_{si} is the series being validated, and N is the sample size. BIA describes the bias of simulated ground temperatures from observed ones in a series. Generally, a

TABLE 1 Descriptions for the control model and experimental models.

Model name	Description
CTRL	The control model, which was forced by *in situ* observed meteorological data in an hourly time step at all stations
CMFD-SR-Exp	A sensitivity experimental model, which was identical to CTRL except that the input downward solar radiation (DSR) in the model was replaced by hourly interpolated CMFD-SR
Tang-SR-Exp	A sensitivity experimental model, which was identical to CTRL except that the input DSR in the model was replaced by hourly interpolated Tang-SR
GLDAS-SR-Exp	A sensitivity experimental model, which was identical to CTRL except that the input DSR in the model was replaced by hourly interpolated GLDAS-SR
CMFD-Ta-Exp	A sensitivity experimental model, which was identical to CTRL except that the input air temperature (Ta) in the model was replaced by hourly interpolated CMFD-Ta
GLDAS-Ta-Exp	A sensitivity experimental model, which was identical to CTRL except that the input Ta in the model was replaced by hourly interpolated GLDAS-Ta
CMFD-Rh-Exp	A sensitivity experimental model, which was identical to CTRL except that the input relative humidity (Rh) in the model was replaced by hourly interpolated CMFD-Rh
GLDAS-Rh-Exp	A sensitivity experimental model, which was identical to CTRL except that the input relative humidity (Rh) in the model was replaced by hourly interpolated GLDAS-Rh
CMFD-Wind-Exp	A sensitivity experimental model, which was identical to CTRL except that the input wind speed (Wind) in the model was replaced by hourly interpolated CMFD-Wind
GLDAS-Wind-Exp	A sensitivity experimental model, which was identical to CTRL except that the input wind speed (Wind) in the model was replaced by hourly interpolated GLDAS-Wind

small absolute BIA means good performance. RMSE presents the overall divergence, or average distance between simulated ground temperatures from observed ones. The lower the RMSE, the better performance a given model achieves. For example, a perfect model will result in an RMSE of 0.

3 | RESULTS

3.1 | Evaluation of the control model

CTRL models were forced by *in situ* observed meteorological data (including both DSR and Ta) at six selected stations. To evaluate the accuracies of CTRL models, the simulated ground temperatures and volumetric soil water (liquid) content were compared with *in situ* observations. For the convenience of visual comparison, hourly series of simulated results and observations were aggregated into daily series, and results are presented in Figures S3–S14 for each station. BIA and RMSE values between the simulated results and *in situ* observations for some selected depths at each station are summarized in Figures 2 and 3. Results show that the simulated ground temperatures are in a good agreement with measurements at most stations, with most RMSE values <1.5°C and all RMSE values <2°C except for the deepest two layers at JYL. All absolute BIA values for the simulated ground temperatures are <0.8°C except for the first layer at ARSF and the deepest two layers at JYL.

Visual inspection of simulated and observed volumetric soil water (liquid) content curves (Figures S4, S6, S8, S10, S12, and S14) shows that the performance of simulated volumetric soil water (liquid) content is not as good as that of simulated ground temperatures. The reasons for this are twofold. First, the simulated soil water (liquid) content in the model is much more sensitive to soil hydraulic parameters, such as porosity, hydraulic conductivity, and pore size distribution index, which were set according to a published dataset without calibration. These parameter values set in the model may be very different from the real field conditions, which may exhibit heterogeneity throughout the landscape and depth profile, and inevitably lead to significant simulation errors. Second, errors in the simulated ground temperatures and uncorrected ground states of alternating freezing or thawing can also lead to significant simulation errors in soil water (liquid) content. For example, an uncorrected early soil thawing in the model would cause an obvious shift in the soil water (liquid) content curve. Overall, the model shows acceptable performance.

3.2 | Validation for DSR and Ta products

The selected 3-hourly DSR and Ta products were compared with *in situ* observations from August 16, 2013 to December 31, 2014, and scatter plots with BIA and RMSE values are shown in Figures 4 and 5. Similar comparisons for the daily means of these products are shown in Figures S15 and S16. BIA, 3-hourly, and daily RMSE against *in situ* observations are summarized in Figures 6 and 7 for DSR and Ta products, respectively.

For DSR products, inferred from the boxplots of BIA and RMSE at all stations (Figure 6d–f), CMFD-SR has the best precision among three selected products. Compared with *in situ* measurements, BIA of CMFD-SR ranges from −20 to 14 W/m^2, with a mean value of −2.89 W/m^2 for all stations. The daily RMSE ranges from 29 to 39 W/m^2 with a mean value of 34.8 W/m^2, and the 3-hourly RMSE ranges from 92 to 114 W/m^2 with a mean value of 103.4 W/m^2. The accuracy of Tang-SR is slightly inferior to that of CMFD-SR, with BIA ranging from −23 to 5 W/m^2 and a mean value of −6.9 W/m^2. Although the 3-hourly RMSE values of Tang-SR differ slightly from those of CMFD-SR, the daily RMSE values range from 34 to 50 W/m^2 with a mean value of 41.5 W/m^2, which are worse than those of

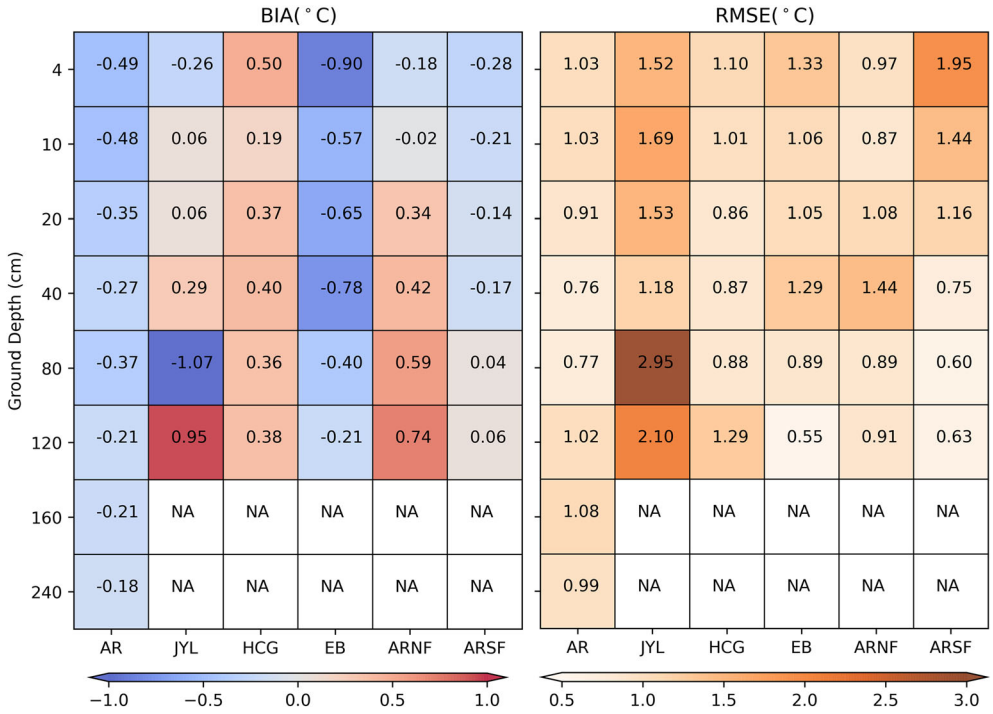

FIGURE 2 BIA (bias) and RMSE (root mean squared error) values for simulated ground temperatures (from August 16, 2013 to December 31, 2014) at various depths by the control model against *in situ* measurements at all stations (AR, JYL, HCG, EB, ARNF, and ARSF). [Colour figure can be viewed at wileyonlinelibrary.com]

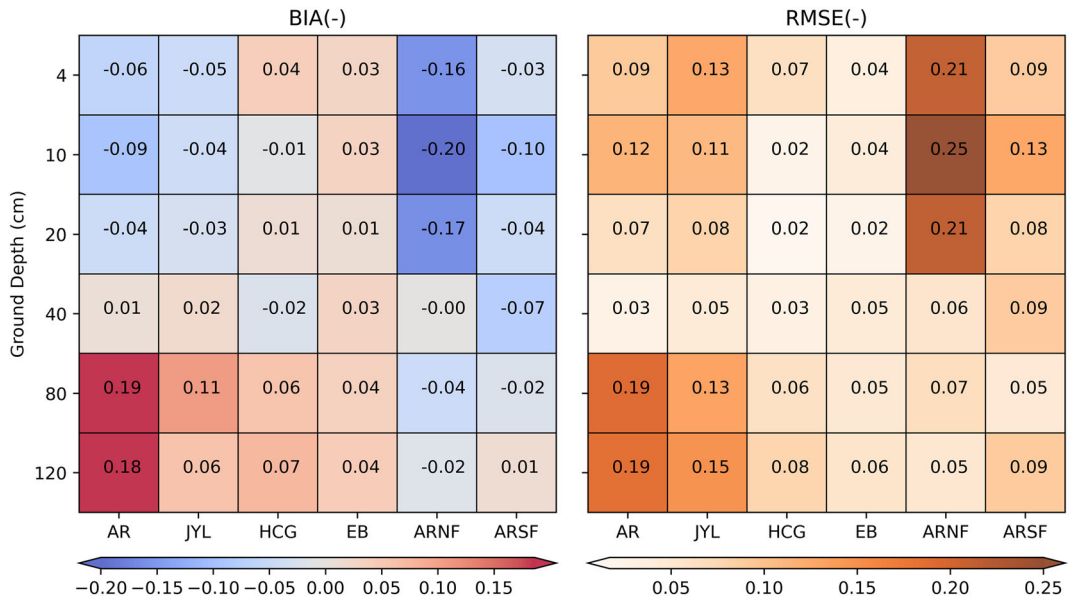

FIGURE 3 BIA (bias) and RMSE (root mean squared error) values for simulated volumetric soil water (liquid) content (from August 16, 2013 to December 31, 2014) at various depths by the control model against *in situ* measurements at all stations (AR, JYL, HCG, EB, ARNF, and ARSF). [Colour figure can be viewed at wileyonlinelibrary.com]

CMFD-SR. For GLDAS-SR, although its daily RMSE values are slightly smaller than those of Tang-SR, its 3-hourly RMSE values are much higher, ranging from 155 to 189 W/m^2 with a mean value of 171.3 W/m^2. Compared to *in situ* observations, GLDAS-SR is obviously underestimated, with BIA ranging from −41 to 1 W/m^2 and a mean value of −17.7 W/m^2 for all stations. In this study, the models ran with an hourly time step. The 3-hourly DSR products were linearly interpolated into hourly series. However, compared to hourly *in situ* observations, the BIA and RMSE of hourly interpolated DSR products differ only slightly from those of 3-hourly series (Figure S17). Linearly interpolated hourly GLDAS-SR in 2014 is compared with hourly *in situ* observations in Figures S18 and S19 for ARNF and ARSF. As shown, there is a systematic underestimation in GLDAS-SR.

Compared to *in situ* observations, the accuracies for both CMFD-Ta and GLDAS-Ta are not very good, and there is no obvious superiority for either product. Air temperature in two selected products is

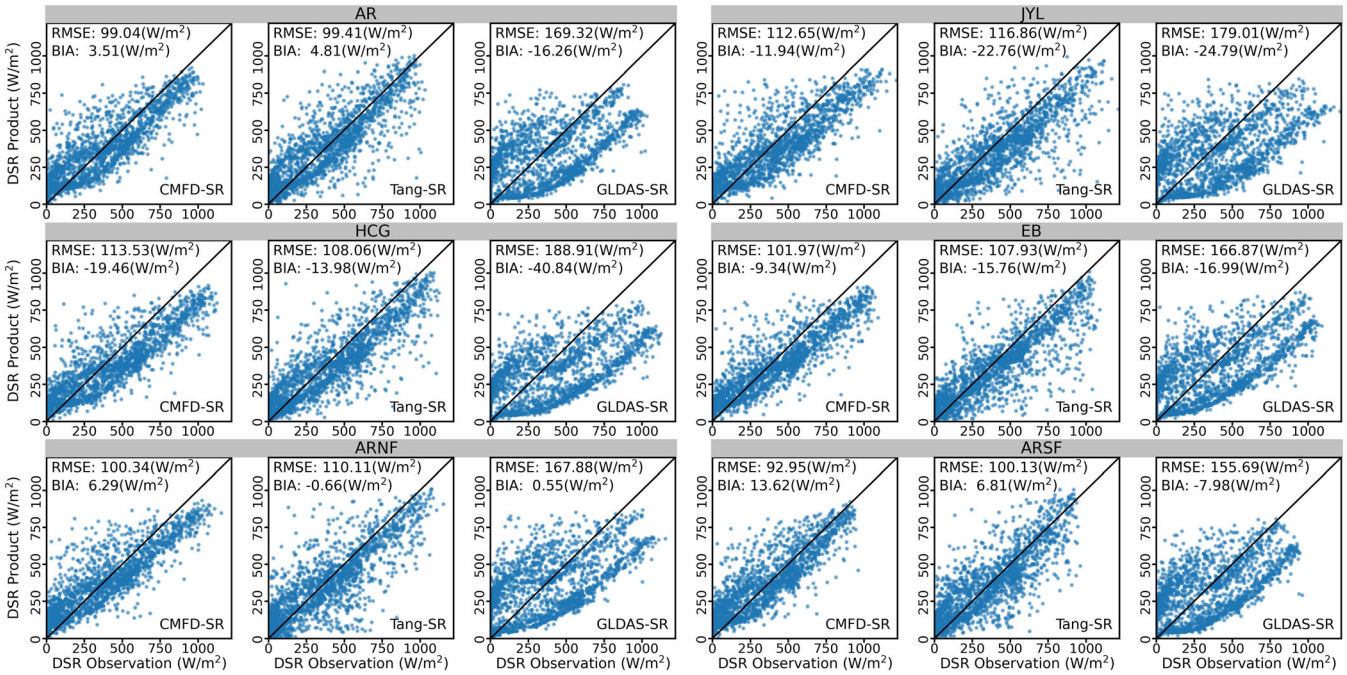

FIGURE 4 Scatter plots between DSR (downward solar radiation) products (CMFD-SR, Tang-SR, and GLDAS-SR, 3-hourly series from August 16, 2013 to December 31, 2014) and *in situ* measurements at all stations (AR, JYL, HCG, EB, ARNF, and ARSF), with BIA (bias) and RMSE (root mean squared error) values presented. [Colour figure can be viewed at wileyonlinelibrary.com]

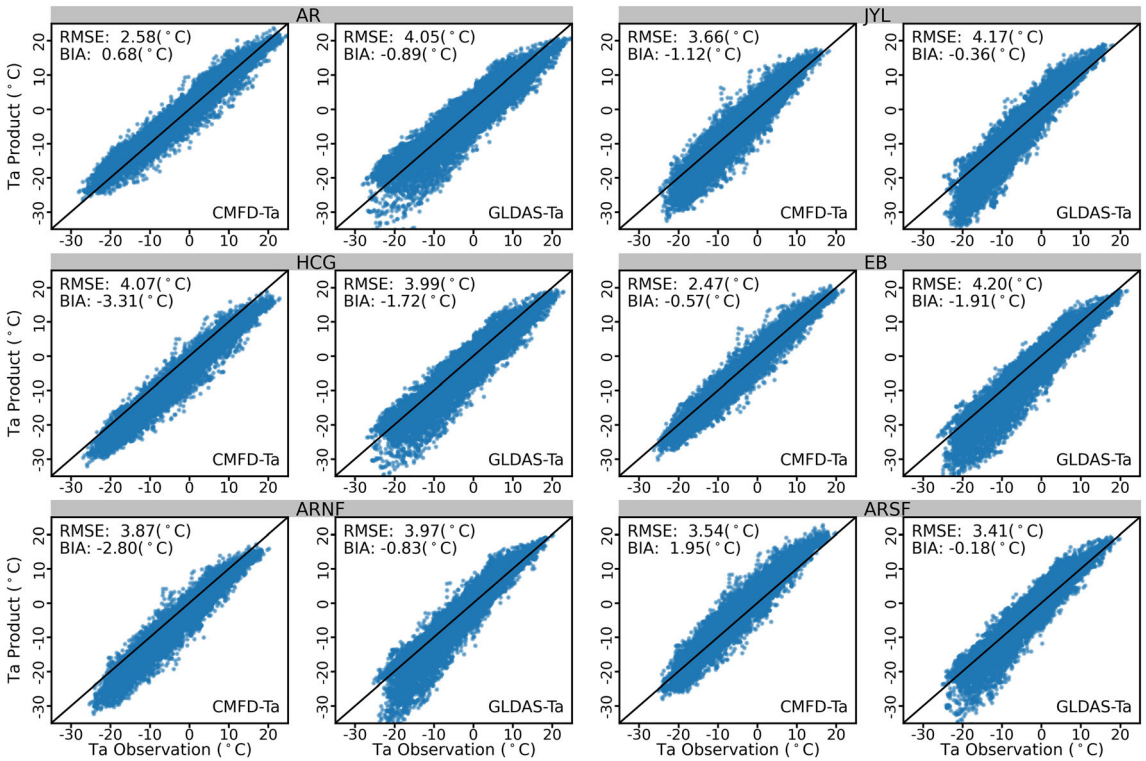

FIGURE 5 Scatter plots between Ta (air temperature) products (CMFD-Ta and GLDAS-Ta, 3-hourly series from August 16, 2013 to December 31, 2014) and *in situ* measurements at all stations (AR, JYL, HCG, EB, ARNF, and ARSF), with BIA (bias) and RMSE (root mean squared error) values presented. [Colour figure can be viewed at wileyonlinelibrary.com]

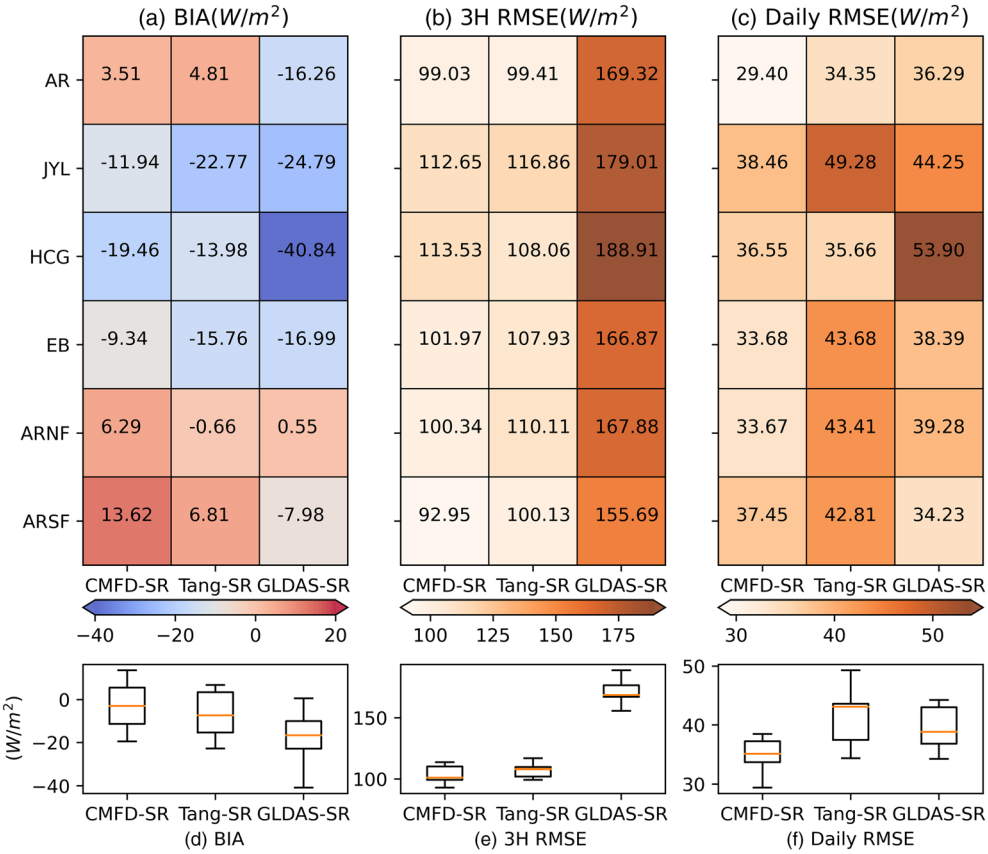

FIGURE 6 BIA (bias) and RMSE (root mean squared error) values for downward solar radiation products (CMFD-SR, Tang-SR, and GLDAS-SR) at all stations (AR, JYL, HCG, EB, ARNF, and ARSF) against *in situ* measurements from August 16, 2013 to December 31, 2014, with boxplots describing the variation in DSR among stations for each product presented in (d–f). (a) and (d) are for BIA values; (b) and (e) are for RMSE values of 3-hourly (3H) series; and (c) and (f) are for RMSE values of daily series. [Colour figure can be viewed at wileyonlinelibrary.com]

generally underestimated, as inferred from significant negative BIA values at most stations (Figure 7). CMFD-Ta has a much larger range in BIA than GLDAS-Ta, with a maximal BIA value of 1.96°C at ARSF and a minimal BIA value of −3.31°C at HCG. Most RMSE values of both CMFD-Ta and GLDAS-Ta are >3°C at most stations, except for those at AR and EB in CMFD-Ta. On average, RMSE values of GLDAS-Ta are higher than those of CMFD-Ta. In addition, the smaller RMSE values (e.g., at AR and EB) in CMFD-Ta are obviously connected with smaller absolute BIA values, and there is no similar pattern for GLDAS-Ta. That is, a smaller BIA of GLDAS-Ta will not assure a better performance when it is used for driving an LSM, because large RMSE values mean an overall large divergence of the Ta product from the real Ta.

3.3 | Sensitivity of simulated ground temperatures to different DSR products

To investigate the influences of DSR products on simulated ground temperatures or thermal state in the model, *in situ* observed DSR in CTRL was substituted with DSR products (i.e., CMFD-SR, Tang-SR, and GLDAS-SR) and other input datasets or parameters were kept identical to CTRL. Then, three experimental models (i.e., CMFD-SR-Exp, Tang-SR-Exp, and GLDAS-SR-Exp) forced by different DSR products were set up. Simulation results of these experimental models were compared directly against the simulation results of CTRL, instead of with *in situ* observations, because the differences between experimental and CTRL models can be assumed to be caused directly by the substitution of DSR. In the long term, there would be systematic deviations between DSR products and measurements, and the inaccuracy or errors in a DSR product would take a long time to propagate downward from the surface and be reflected in the ground temperatures at depth when it was used to force LSMs. Therefore, all experimental models ran for 10 years repeatedly with the meteorological data of 2014 and the results in the last year were compared with the counterpart of the 10-year version of CTRL. After a 10-year model run, the simulated ground temperatures at selected depths at all stations in CTRL and experimental models are compared and illustrated in Figures S20–S25.

Compared to CTRL, the simulated ground temperatures were obviously underestimated in GLDAS-SR-Exp at most stations, especially in warm seasons. Differences in simulated maximum (corresponding to warm seasons) and minimum (corresponding to cold seasons) ground temperatures between the experimental and CTRL models are summarized in Figures S26 and S27. As shown in Figure S26C, the maximal ground temperatures simulated in GLDAS-SR-Exp were greatly underestimated at most stations compared to CTRL. At ARNF, they were decreased by about −4°C. The reason is that GLDAS-SR is much lower than *in situ* measurements at most stations (see Figures S18 and S19, and BIA values in Figure 6). However, the differences in simulated maximal ground temperatures between CMFD-SR-Exp/Tang-SR-Exp and CTRL were relatively smaller, although they were also underestimated at some stations.

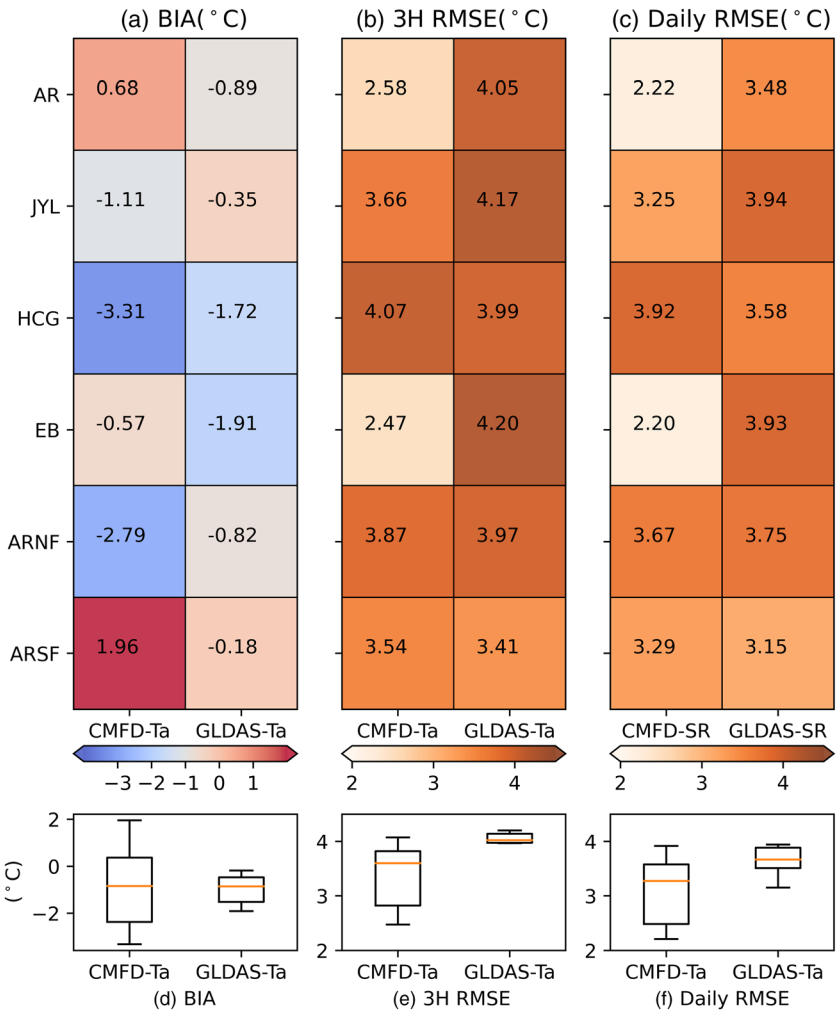

FIGURE 7 BIA (bias) and RMSE (root mean squared error) values for air temperature products (CMFD-Ta and GLDAS-Ta) at all stations (AR, JYL, HCG, EB, ARNF, and ARSF) against *in situ* measurements from August 16, 2013 to December 31, 2014, with boxplots describing the variation in Ta among stations for each product presented in (d–f). (a) and (d) are for BIA values; (b) and (e) are for RMSE values of 3-hourly (3H) series; and (c) and (f) are for RMSE values of daily series. [Colour figure can be viewed at wileyonlinelibrary.com]

Figures S20–S25 also indicate that the simulated ground temperatures in CMFD-SR-Exp and Tang-SR-Exp are relatively closer to CTRL than those in GLDAS-SR-Exp. The differences in simulated minimal ground temperatures between the three experimental models and CTRL were relatively smaller than those in maximal ground temperatures among CMFD-SR-Exp, Tang-SR-Exp, and GLDAS-SR-Exp.

BIA and RMSE values of simulated ground temperatures in three experimental models against CTRL are listed in Figures 8 and 9. The absolute BIA and RMSE values of CMFD-SR-Exp and Tang-SR-Exp are much smaller than those of GLDAS-SR-Exp, suggesting that CMFD-SR-Exp and Tang-SR-Exp show a better performance than GLDAS-SR-Exp. The BIA values between all experimental models and CTRL differ slightly with depth along the vertical profile at all stations, indicating that the inaccuracy or errors in DSR products have been fully propagated to deep layers. RMSE shows a similar pattern along the vertical profile, although it decreases slightly with depth, which is presumably caused by the dampening effect of ground or soil.

Mean values of BIA and RMSE at all depths (e.g., the mean of BIA/RMSE values in a column in Figure 8a–c or 9a–c) were calculated along the entire vertical profile for each station for the simulated ground temperatures between experimental models and CTRL. Figure 10 shows that the mean values of BIA and RMSE for simulated ground temperatures are closely related to errors (i.e., BIA or RMSE against *in situ* observations) in DSR products. Generally, a larger absolute BIA in DSR could lead to a higher absolute mean BIA in the simulated ground temperatures in experimental models. Most mean values of absolute BIA for simulated ground temperatures in CMFD-SR-Exp and Tang-SR-Exp are much smaller than those in GLDAS-SR-Exp, and there are no apparent advantages between CMFD-SR-Exp and Tang-SR-Exp. However, from the perspective of RMSE, CMFD-SR-Exp tends to show a slightly better performance than Tang-SR-Exp and GLDAS-SR-Exp.

Although the relationship between the daily RMSE of DSR and the mean RMSE of simulated ground temperatures along the vertical profile is inconspicuous, 3-hourly DSR products with lower RMSE obviously lead to lower mean RMSE for simulated ground temperatures in experimental models (Figure 10c). The RMSE of 3-hourly CMFD-SR and Tang-SR at most stations ranges from 100 to 120 W/m^2, leading to a mean RMSE value of about 0.5–0.75°C for the simulated ground temperatures. However, the RMSE of 3-hourly GLDAS-SR is >160 W/m^2 at most stations, and the mean RMSE is >1°C for simulated ground temperatures in GLDAS-SR-Exp at most stations, except for JYL with a mean RMSE of 0.29°C, which could be explained by the occurrence of permafrost, because permafrost

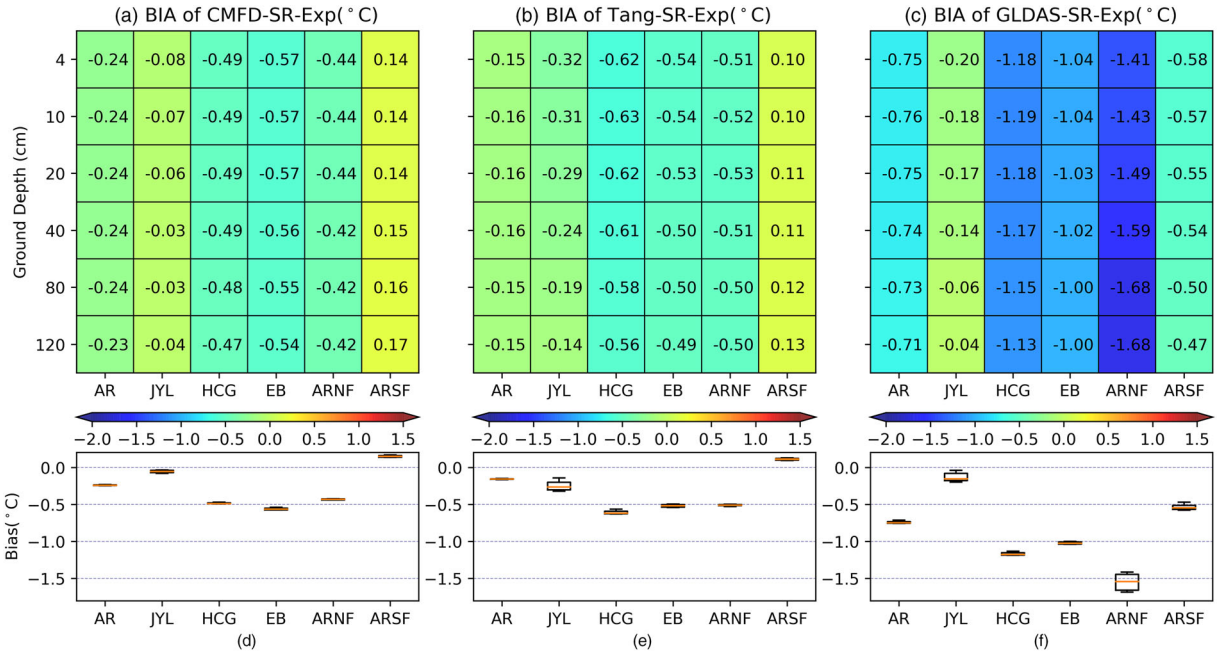

FIGURE 8 (a) BIA (bias) values for simulated ground temperatures at various depths in the last year after a 10-year model running by CMFD-SR-Exp against the control model at all stations (AR, JYL, HCG, EB, ARNF, and ARSF). (b) The same as A except that it is for Tang-SR-Exp. (c) The same as a except that it is for GLDAS-SR-Exp. Boxplots for each experimental model (d for CMFD-SR-Exp, e for Tang-SR-Exp, and f for GLDAS-SR-Exp) describing the variation in BIA among various depths at each station are presented in (d–f). [Colour figure can be viewed at wileyonlinelibrary.com]

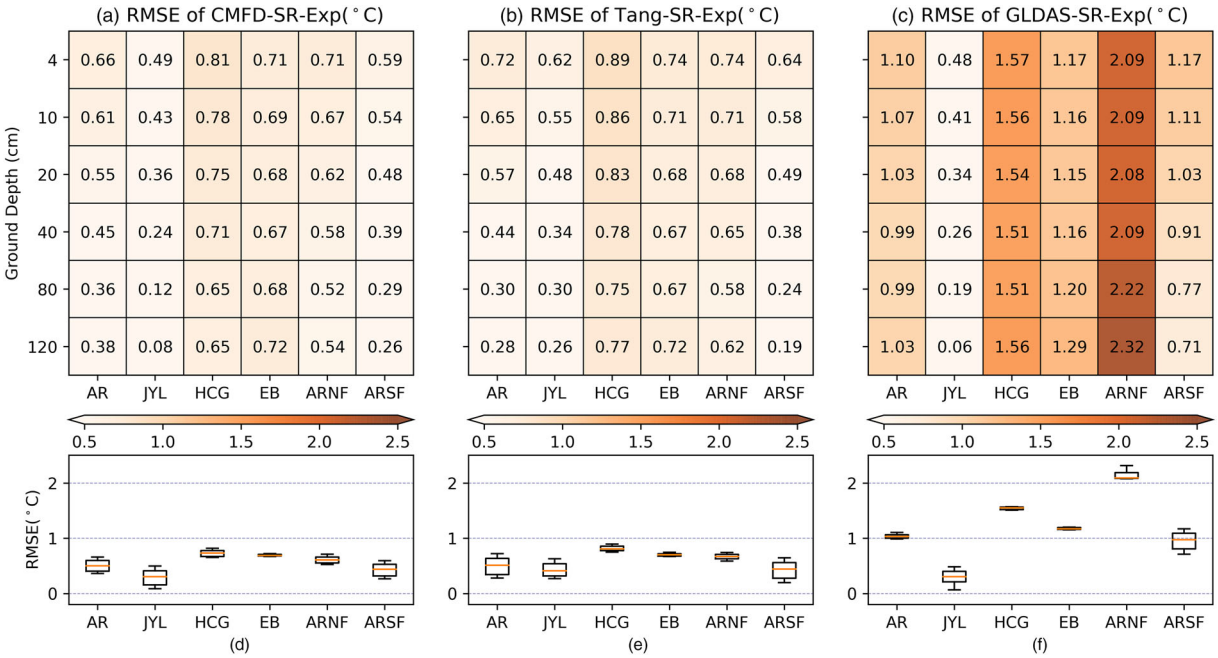

FIGURE 9 (a) RMSE (root mean squared error) values for simulated ground temperatures at various depths in the last year after a 10-year model running by CMFD-SR-Exp against the control model at all stations (AR, JYL, HCG, EB, ARNF, and ARSF). (b) The same as a except that it is for Tang-SR-Exp. (c) The same as a except that it is for GLDAS-SR-Exp. Boxplots for each experimental model (d for CMFD-SR-Exp, e for Tang-SR-Exp, and f for GLDAS-SR-Exp) describing the variation in RMSE among various depths at each station are presented in (d–f). [Colour figure can be viewed at wileyonlinelibrary.com]

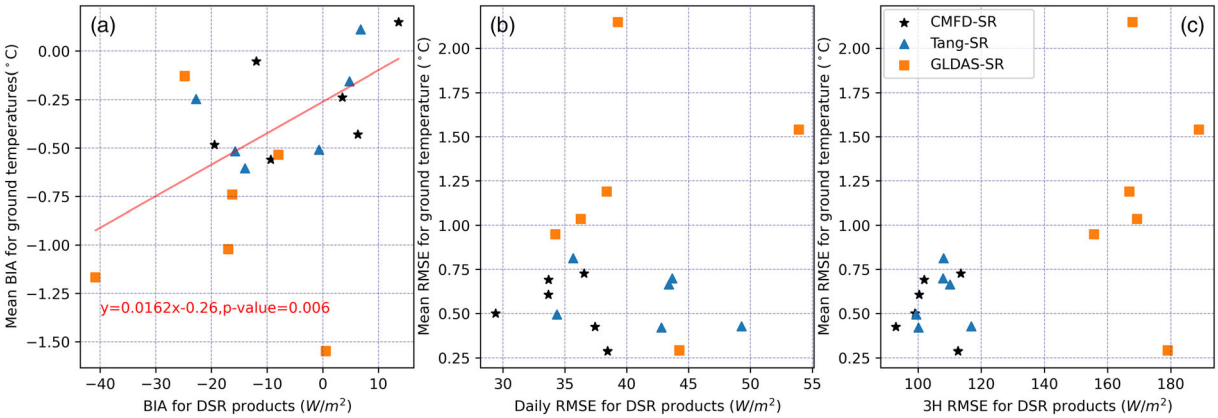

FIGURE 10 Relationship between mean BIA (bias)/RMSE (root mean squared error) at all depths (e.g., the mean of BIA/RMSE values in a column in Figures 8a–c or 9a–c) for simulated ground temperatures in each experimental model and the BIA/RMSE of DSR (downward solar radiation) products at all stations (each point stands for one station). All BIA or RMSE values are calculated based on the data from the last year of the 10-year model running. (a) Relationship between mean BIA at all depths for simulated ground temperatures in experimental models (CMFD-SR-Exp, Tang-SR-Exp, and GLDAS-SR-Exp) and BIA of DSR products (CMFD-SR, Tang-SR, and GLDAS-SR); (b) relationship between mean RMSE at all depths for simulated ground temperatures and daily RMSE of DSR products; (c) relationship between mean RMSE at all depths for simulated ground temperatures and 3-hourly RMSE of DSR products. [Colour figure can be viewed at wileyonlinelibrary.com]

thawing can absorb large amounts of heat and substantially dampen the propagation of ground temperature variation downward from the surface. Therefore, it is also difficult for an error or change in DSR to affect the deep ground temperatures in permafrost before it thaws. In short, a BIA of −20 W/m^2 in CMFD-SR or Tang-SR will lead to a BIA of about −0.5°C in the simulated ground temperatures, and an RMSE of about 100–120 W/m^2 in 3-hourly DSR products will result in an RMSE of about 0.5–0.75°C in the simulated ground temperatures.

3.4 | Sensitivity of simulated ground temperatures to different Ta products

Both CMFD and GLDAS (which have 3-hour Ta products) were linearly interpolated into hourly series and used to force SHAWDHM as a replacement of *in situ* observed Ta in CTRL, and other inputs and parameters were kept unchanged. Then, two experimental models (i.e., CMFD-Ta-Exp and GLDAS-Ta-Exp) were obtained. As with DSR model runs, to guarantee that impacts of inaccuracy or errors in Ta products were fully reflected in the simulated ground temperatures, CMFD-Ta-Exp and GLDAS-Ta-Exp ran repeatedly for 10 years with the meteorological data of 2014, and results of the last year were compared with the 10-year version of CTRL, illustrated in Figures S28–S33. Differences in simulated maximal and minimal ground temperatures between CMFD-Ta-Exp/GLDAS-Ta-Exp and CTRL are also summarized in Figures S34 and S35.

The BIA and RMSE values of CMFD-Ta and GLDAS-Ta against *in situ* observations at all stations in 2014 are presented in the first rows in Figures 11 and 12. As shown, both CMFD-Ta and GLDAS-Ta have obvious BIA against *in situ* measurements (also see Figure 7), and most absolute BIA values are >1°C. In general, the performance of CMFD-Ta-Exp and GLDAS-Ta-Exp in simulating ground temperatures was worse than that of CMFD-SR-Exp and GLDAS-SR-Exp, resulting in higher BIA and RMSE values. For example, most absolute BIA values of simulated ground temperatures in CMFD-Ta-Exp and GLDAS-Ta-Exp are >1°C, and some are even >1.5 or 2°C (Figure 11a and b).

The mean BIA of all depths (i.e., the mean of BIA values in a column except the first row in Figure 11a and b) for simulated ground temperatures along the entire vertical profile in CMFD-Ta-Exp and GLDAS-Ta-Exp is highly related to BIA in CMFD-Ta or GLDAS-Ta, and they are in close linear relationship (Figure 11c, $p < 0.001$). On average, every 1°C of BIA in the input Ta product will lead to a BIA of 0.72°C in the simulated ground temperatures, and neither CMFD-Ta-Exp nor GLDAS-Ta-Exp has a significant superiority to each other in performance (Figure 11c). The first row of Figure 12a and b illustrates RMSE values of CMFD-Ta and GLDAS-Ta against *in situ* measurements, and the rest rows present RMSE values of simulated ground temperatures in CMFD-Ta-Exp and GLDAS-Ta-Exp against CTRL. As shown, almost all RMSE values for these two Ta products are greater than 2°C, even greater 3°C at some stations. Due to the inadequate accuracies (e.g., high BIA and RMSE values) in the selected Ta products, most RMSE values of simulated ground temperatures in CMFD-Ta-Exp and GLDAS-Ta-Exp are higher than 1°C, which are much worse than those in CMFD-SR-Exp and Tang-SR-Exp. In general, a Ta product with higher RMSE would lead to higher RMSE values in simulated ground temperatures. However, the linear relationship between RMSE of Ta and mean RMSE of simulated ground temperatures along the entire vertical profile is not obvious. In contrast, the mean RMSE of all depths for simulated ground temperatures has a stronger linear relationship with absolute BIA of Ta products, as shown in Figure 13.

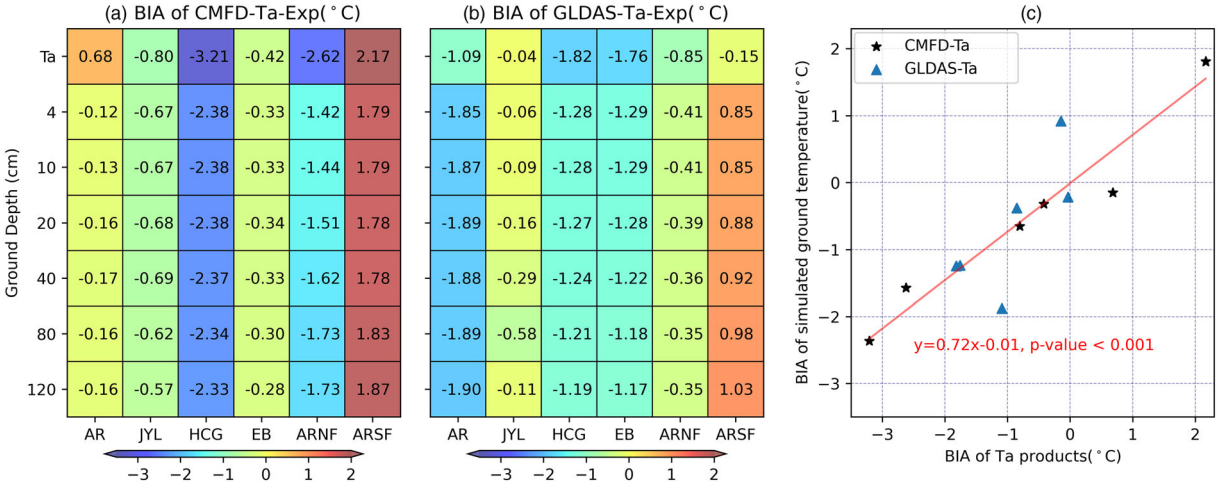

FIGURE 11 (a) BIA (bias) values for Ta (air temperature) product (e.g., the first row shows BIA values for CMFD-Ta) and simulated ground temperatures at various depths (all except the first row) by CMFD-Ta-Exp against the control model at all stations (AR, JYL, HCG, EB, ARNF, and ARSF); (b) the same as A except that it is for GLDAS-Ta and GLDAS-Ta-Exp; (c) relationship between mean BIA at all depths (i.e., the mean of BIA values in a column except the first row in A and B) for simulated ground temperatures and BIA (the first row in A and B) for Ta products (CMFD-Ta and GLDAS-Ta), each point standing for one station. Note that all BIA values are calculated based on the data from the last year of the 10-year model running. [Colour figure can be viewed at wileyonlinelibrary.com]

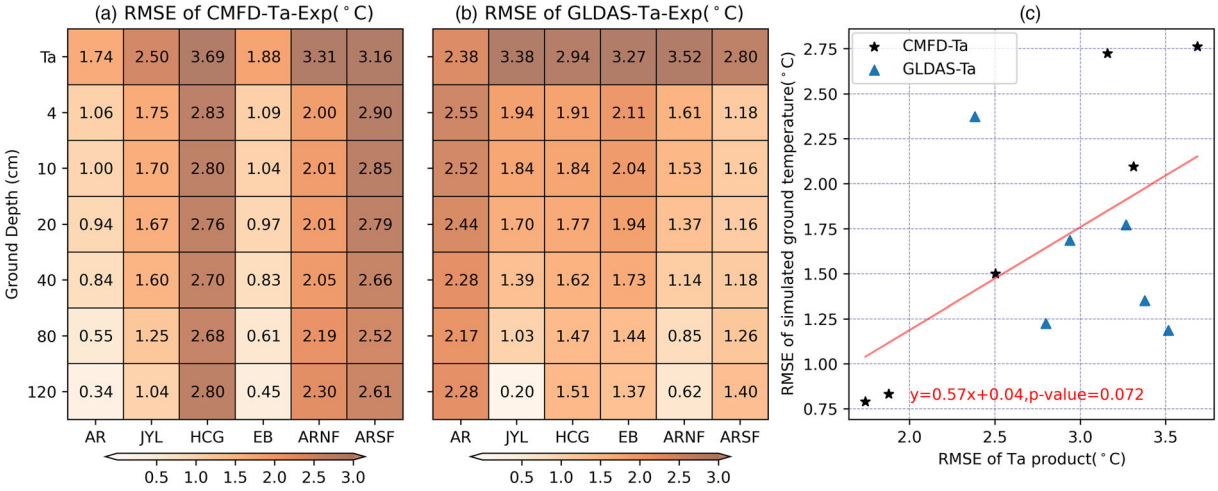

FIGURE 12 (a) RMSE (root mean squared error) values for Ta (air temperature) product (e.g., the first row shows RMSE values for CMFD-Ta) and simulated ground temperatures at various depths by CMFD-Ta-Exp against the control model at all stations (AR, JYL, HCG, EB, ARNF, and ARSF); (b) the same as A except that it is for GLDAS-Ta and GLDAS-Ta-Exp; (c) relationship between the mean RMSE at all depths (i.e., the mean of RMSE values in a column except the first row in A and B) for simulated ground temperatures and RMSE (the first row in A and B) for Ta products (CMFD-Ta and GLDAS-Ta), each point standing for one station. Note that all RMSE values are calculated based on the data from the last year of the 10-year model running. [Colour figure can be viewed at wileyonlinelibrary.com]

4 | DISCUSSION

According to the simulation results, CMFD-SR and Tang-SR are good alternatives to *in situ* observed DSR for forcing LSMs in remote areas with scarce solar radiation observations, with acceptable accuracies in simulated ground temperatures. For example, most absolute BIA and RMSE values of simulated ground temperatures in CMFD-SR-Exp and Tang-SR-Exp against CTRL are <0.6 and 0.9°C, respectively. However, simulated ground temperatures are far more sensitive to the substitution of Ta than the substitution of DSR. Using either CMFD-Ta or GLDAS-Ta, the model resulted in much larger errors in the simulated ground temperatures. The study area has a rugged terrain with dramatic variation in elevation, which leads to significant variation in Ta with altitude and results in many challenges for obtaining accurate estimation of spatially distributed Ta. The results in this study are useful for understanding the impacts of an atmospheric forcing dataset on simulated ground temperatures and thermal state, and help interpret simulation results and conclusions, which should be carefully

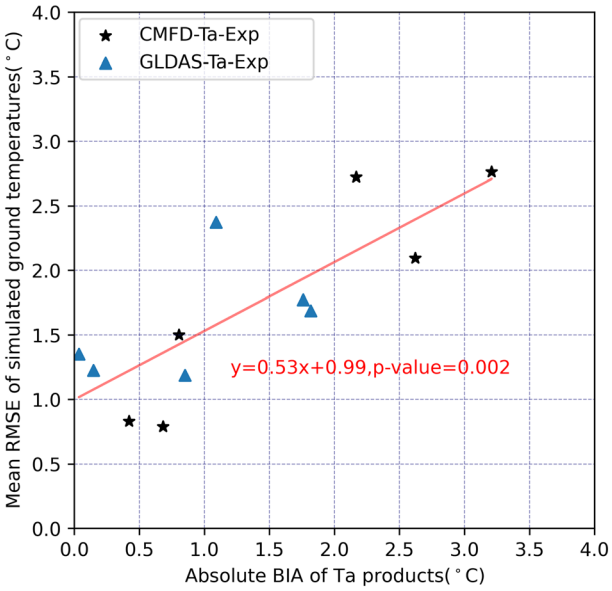

FIGURE 13 Relationship between mean RMSE (root mean squared error) at all depths (e.g., mean of RMSE values in a column except the first row in Figure 12a and b) for simulated ground temperatures in experimental models (CMFD-Ta-Exp and GLDAS-Ta-Exp) and absolute BIA of air temperature products (CMFD-Ta and GLDAS-Ta), each point standing for one station. Note that all RMSE and BIA values are calculated based on the data from the last year of the 10-year model running. [Colour figure can be viewed at wileyonlinelibrary.com]

considered when LSMs are driven by various Ta products, instead of observations.

There are still some aspects that have not been considered in this study, which may limit the range of applicability of the analysis results.

First, there are many LSMs (e.g., Common Land Model and Community Land Model)[25,71] prevailing in the current community. Although the governing equations for heat transfer in the ground are nearly the same in most models, model structure, parameterization schemes, and components (e.g., boundary conditions, residue, canopy, snowpack) and algorithms (e.g., ground heat flux from the surface and other boundary conditions) for the boundary layer may differ significantly.[72] For example, the impacts of residue and shadows cast by surrounding terrain were considered in SHAWDHM, but they are often ignored in other LSMs.[71] The consequence is that the difference in simulated ground temperatures between LSMs would be considerable, even when the models are driven by the same forcing dataset.[73] In turn, responses of simulated ground temperatures to the substitution of Ta or DSR by products would also differ in different LSMs, and model intercomparisons were not conducted in this study or found in the literature. There are some similar sensitivity analyses of terrestrial evapotranspiration (ET) to the choices of forcing datasets. The most sensitive variables that drive the difference in simulated ET are very different between models.[74,75] That is, when another LSM was used, the results could be different from this study, depending on the model structure and implementations.

Second, analysis in this study was limited to investigating the impacts of uncertainties in forcing datasets on simulated ground temperatures, and did not attempt to reproduce to the occurrence of permafrost (i.e., permafrost distribution). Numerical experiments were conducted only at six stations, and five of them are located in seasonally frozen ground, only one in permafrost. Although all experimental models reproduced the permafrost occurrence at JYL, the influence of forcing dataset choice on permafrost distribution in the study area was not investigated explicitly.

Third, only either Ta or DSR was substituted with products in experimental models, and other forcing variables (e.g., air humidity, wind speed, and precipitation) were not included in this study. Because the soil water transfer is deeply coupled to heat transfer, the impacts of precipitation on ground temperatures or thermal state would be significant. Generally, the impacts from precipitation are complicated, and they could be imposed through various paths, including heat convection of rain, soil moisture (related to thermal capacity, conductivity, and phase change), ET, and snow cover.[76] As reported, in GLDAS runs driven by different precipitation products, the percentage differences in volumetric soil water content (SWC) ranged from −75 to +100%, and the soil temperature spread between simulations ranged up to ±3.0 K.[77] Substitution of air humidity, pressure, and wind speed in LSMs would also have obvious influences on the simulation results, although they would be much smaller than those from the substitution of Ta and DSR (similar results are listed in Figures S36 and S37 for models CMFD-Rh-Exp, GLDAS-Rh-Exp, CMFD-Wind-Exp, and GLDAS-Wind-Exp, forced by wind speed and relative humidity products from CMFD and GLDAS). In addition, only one forcing variable was substituted by products at each time in the experimental models, and the influences of product combinations of multiple forcing variables were not investigated. In fact, in many LSM simulations or projections, input meteorological data were often chosen from a single dataset, and simulation results may differ when different datasets were chosen. For example, obvious discrepancies in simulated temporal changes of permafrost area (−5.8 to −9.0%) and active layer thickness (9.9–20.2%) have been reported when different atmospheric forcing datasets were used to drive the community land model (CLM).[78]

5 | CONCLUSIONS

DSR and Ta have significant influences on the thermal state of frozen ground. They are also important forcing terms with crucial impacts on ground temperature simulation in physically based LSMs, which are useful quantitative analysis tools and have often been widely used for permafrost mapping and predicting the responses of frozen ground to climate change. However, the accuracies of spatially distributed input forcing datasets are vital to the simulation results, especially at regional or continental scales.

In this study, three selected DSR products and two Ta products were first evaluated against *in situ* observations at six stations in an alpine watershed in West China. Then, a physically based land surface model (i.e., SHAWDHM) was driven by *in situ* observed meteorological data, and validated against measurements at these stations (the validated model is namely called CTRL). Finally, some experimental models were modulated from CTRL by substituting the *in situ* observed DSR or Ta by one of various selected products each time (CMFD-SR, Tang-SR, and GLDAS-SR for DSR, and CMFD-Ta and GLDAS-Ta for Ta), and sensitivities of simulated ground temperatures to the substitutions were analysed by comparing the results of experimental models with those of CTRL. Validation shows that SHAWDHM has good performance in simulating ground temperatures.

Among the three selected DSR products, CMFD-SR has the best accuracy with smaller absolute BIA and RMSE values. Tang-SR is slightly inferior to CMFD-SR, with slightly higher absolute BIA and 3-hourly RMSE values, and much higher daily RMSE values. Both CMFD-SR and Tang-SR are far superior to GLDAS-SR, which has significantly higher BIA and RMSE values. In addition, in GLDAS-SR, the DSR is systematically underestimated at all six stations. When they are used to force SHAWDHM, the simulated ground temperatures in GLDAS-SR-Exp were obviously underestimated at most stations, especially in warm seasons. In the meantime, the deviations of CMFD-SR-Exp and Tang-SR-Exp from CTRL are not very significant, with much smaller absolute BIA and RMSE values for most stations. In addition, there is no apparent advantage between CMFD-SR and Tang-SR for forcing SHAWDHM. That is, either CMFD-SR or Tang-SR could be a good alternative to *in situ* observation to force an LSM in remote areas with no DSR observation, resulting in acceptable errors in simulated ground temperatures.

Both CMFD-Ta and GLDAS-Ta at most stations have significant discrepancies from *in situ* observations (with large BIA and RMSE values), which inevitably leads to significant errors in simulated ground temperatures. In general, the results of CMFD-Ta-Exp and GLDAS-Ta-Exp were overall worse than those in CMFD-SR-Exp and Tang-SR-Exp. The simulated ground temperatures in SHAWDHM were much more sensitive to the substitution of observed Ta by a Ta product than the substitution of DSR. That is, for some results or conclusions related to simulated ground temperatures or thermal state of frozen ground, more care should be paid when an LSM is driven by using a Ta product instead of observed air temperature series.

ACKNOWLEDGEMENTS

This article was edited by Professor Mauro Guglielmin. We thank the editors and anonymous reviewers for their comments and constructive suggestions. This work was supported by the National Natural Science Foundation of China (Grant Nos. 41971079 and 41671059; 41975081) and Strategic Priority Research Program of the Chinese Academy of Sciences (Grant No. XDA20100103). The datasets used in this study were provided by the National Tibetan Plateau/Third Pole Environment Data Center (http://data.tpdc.ac.cn/en/).

CONFLICT OF INTEREST STATEMENT

The authors have no conflicts of interest.

DATA AVAILABILITY STATEMENT

Data sharing is not applicable to this article as no new data were created or analyzed in this study.

ORCID

Yanlin Zhang https://orcid.org/0000-0002-2370-7215

REFERENCES

1. Biskaborn BK, Smith SL, Noetzli J, et al. Permafrost is warming at a global scale. *Nat Commun*. 2019;10(1):264. doi:10.1038/s41467-018-08240-4
2. Chang X, Jin H, He R, et al. Permafrost changes in the northwestern Da Xing'anling mountains, Northeast China, in the past decade. *Earth Syst Sci Data*. 2022;14(9):3947-3959. doi:10.5194/essd-14-3947-2022
3. Jin H, Jin X, He R, et al. Evolution of permafrost in China during the last 20 ka. *Sci China Earth Sci*. 2019;62(8):1207-1223. doi:10.1007/s11430-018-9272-0
4. Ran Y, Li X, Cheng G, et al. New high-resolution estimates of the permafrost thermal state and hydrothermal conditions over the northern hemisphere. *Earth Syst Sci Data*. 2022;14(2):865-884. doi:10.5194/essd-14-865-2022
5. Li X, Jin H, Sun L, et al. Climate warming over 1961-2019 and impacts on permafrost zonation in Northeast China. *J Forest Res*. 2022;33(3):767-788. doi:10.1007/s11676-021-01403-y
6. Schuur EAG, Mack MC. Ecological response to permafrost thaw and consequences for local and global ecosystem services. *Annu Rev Ecol Evol Syst*. 2018;49(1):279-301. doi:10.1146/annurev-ecolsys-121415-032349
7. Ala-Aho P, Autio A, Bhattacharjee J, et al. What conditions favor the influence of seasonally frozen ground on hydrological partitioning? A systematic review. *Environ Res Lett*. 2021;16(4):043008. doi:10.1088/1748-9326/abe82c
8. Li X, Cheng G, Ge Y, et al. Hydrological cycle in the Heihe River basin and its implication for water resource management in endorheic basins. *J Geophys Res Atmos*. 2018;123(2):890-914. doi:10.1002/2017JD027889
9. Li X, Zhang L, Zheng Y, et al. Novel hybrid coupling of ecohydrology and socioeconomy at river basin scale: a watershed system model for the Heihe River basin. *Environ Model Software*. 2021;141:105058. doi:10.1016/j.envsoft.2021.105058
10. Luo D, Guo D, Jin H, Yang S, Phillips MK, Frey B. Editorial: ecological impacts of degrading permafrost. *Front Earth Sci*. 2022;10. doi:10.3389/feart.2022.967530
11. Mu C, Abbott BW, Norris AJ, et al. The status and stability of permafrost carbon on the Tibetan plateau. *Earth-Science Rev*. 2020;211:103433. doi:10.1016/j.earscirev.2020.103433
12. Schuur EAG, McGuire AD, Schädel C, et al. Climate change and the permafrost carbon feedback. *Nature*. 2015;520(7546):171-179. doi:10.1038/nature14338
13. Luo DL, Jin HJ, He RX, et al. Characteristics of water-heat exchanges and inconsistent surface temperature changes at an elevational permafrost site on the Qinghai-Tibet plateau. *J Geophys Res Atmos*. 2018;123(18):10057-10075. doi:10.1029/2018JD028298
14. Luo D, Jin H, Wu Q, et al. Thermal regime of warm-dry permafrost in relation to ground surface temperature in the source areas of the Yangtze and yellow rivers on the Qinghai-Tibet plateau, SW China. *Sci Total Environ*. 2018;618:1033-1045. doi:10.1016/j.scitotenv.2017.09.083

15. Luo D, Liu L, Jin H, Wang X, Chen F. Characteristics of ground surface temperature at Chalaping in the source area of the Yellow River, northeastern Tibetan plateau. *Agric fFor Meteorol*. 2020;281:107819. doi:10.1016/j.agrformet.2019.107819
16. Zhao L, Wu Q, Marchenko SS, Sharkhuu N. Thermal state of permafrost and active layer in Central Asia during the international polar year. *Permafr Periglac Process*. 2010;21(2):198-207. doi:10.1002/ppp.688
17. Chang X, Jin H, Zhang Y, et al. Thermal impacts of boreal forest vegetation on active layer and permafrost soils in northern Da Xing'Anling (Hinggan) mountains, Northeast China. *Arctic Antarctic Alpine Res*. 2015;47(2):267-279. doi:10.1657/AAAR00C-14-016
18. Zou D, Zhao L, Sheng Y, et al. A new map of permafrost distribution on the Tibetan plateau. *Cryosphere*. 2017;11(6):2527-2542. doi:10.5194/tc-11-2527-2017
19. Wu Q, Zhang T, Liu Y. Permafrost temperatures and thickness on the Qinghai-Tibet plateau. *Global Planet Change*. 2010;72(1):32-38. doi:10.1016/j.gloplacha.2010.03.001
20. Lacelle D, Lapalme C, Davila AF, et al. Solar radiation and air and ground temperature relations in the cold and hyper-arid Quartermain Mountains, McMurdo dry valleys of Antarctica. *Permafr Periglac Process*. 2016;27(2):163-176. doi:10.1002/ppp.1859
21. Williams TJ, Quinton WL. Modelling incoming radiation on a linear disturbance and its impact on the ground thermal regime in discontinuous permafrost. *Hydrol Process*. 2013;27(13):1854-1865. doi:10.1002/hyp.9792
22. Hoelzle M. Permafrost occurrence from BTS measurements and climatic parameters in the eastern Swiss Alps. *Permafr Periglac Process*. 1992;3(2):143-147. doi:10.1002/ppp.3430030212
23. Gruber S, Fleiner R, Guegan E, et al. Review article: inferring permafrost and permafrost thaw in the mountains of the Hindu Kush Himalaya region. *Cryosphere*. 2017;11(1):81-99. doi:10.5194/tc-11-81-2017
24. Niu GY, Yang ZL. Effects of frozen soil on snowmelt runoff and soil water storage at a continental scale. *J Hydrometeorol*. 2006;7(5):937-952. doi:10.1175/JHM538.1
25. Dai Y, Zeng X, Dickinson RE, et al. The common land model. *Bull AAm Meteorol Soc*. 2003;84(8):1013-1024. doi:10.1175/bams-84-8-1013
26. Guo D, Wang H. Simulated historical (1901-2010) changes in the permafrost extent and active layer thickness in the northern hemisphere. *J Geophys Res Atmos*. 2017;122(22):12,285-212,295. doi:10.1002/2017JD027691
27. Guo D, Wang H. CMIP5 permafrost degradation projection: a comparison among different regions. *J Geophys Res Atmos*. 2016;121(9):4499-4517. doi:10.1002/2015JD024108
28. Zhang Y, Cheng G, Li X, et al. Influences of frozen ground and climate change on hydrological processes in an alpine watershed: a case study in the upstream area of the Hei'he river, Northwest China. *Permafr Periglac Process*. 2017;28(2):420-432. doi:10.1002/ppp.1928
29. Garen DC, Marks D. Spatially distributed energy balance snowmelt modelling in a mountainous river basin: estimation of meteorological inputs and verification of model results. *J Hydrol*. 2005;315(1):126-153. doi:10.1016/j.jhydrol.2005.03.026
30. Klug C, Rieg L, Ott P, Mössinger M, Sailer R, Stötter J. A multi-methodological approach to determine permafrost occurrence and ground surface subsidence in mountain terrain, Tyrol, Austria. *Permafr Periglac Process*. 2017;28(1):249-265. doi:10.1002/ppp.1896
31. McVicar TR, Van Niel TG, Li L, Hutchinson MF, Mu X, Liu Z. Spatially distributing monthly reference evapotranspiration and pan evaporation considering topographic influences. *J Hydrol*. 2007;338(3):196-220. doi:10.1016/j.jhydrol.2007.02.018
32. Dozier J. A clear sky spectral solar radiation model for snow covered mountainous terrain. *Water Resour Res*. 1980;16(4):709-718. doi:10.1029/WR016i004p00709
33. Zhang YL, Li X, Cheng GD, et al. Influences of topographic shadows on the thermal and hydrological processes in a cold region mountainous watershed in Northwest China. *J Adv Model Earth Syst*. 2018;10(7):1439-1457. doi:10.1029/2017MS001264
34. Zhang X, Huang A, Dai Y, et al. Influences of 3D sub-grid terrain radiative effect on the performance of CoLM over Heihe River bBasin, Tibetan pPlateau. *J Adv Model Earth Syst*. 2022;14(1):e2021MS002654. doi:10.1029/2021MS002654
35. Zhang Y, Chang X, Liang J. Comparison of different algorithms for calculating the shading effects of topography on solar irradiance in a mountainous area. *Environ Earth Sci*. 2017;76(7):295. doi:10.1007/s12665-017-6618-5
36. Ma Y, Pinker RT, Wonsick MM, Li C, Hinkelman LM. Shortwave radiative fluxes on slopes. *J Appl Meteorol Climatol*. 2016;55(7):1513-1532. doi:10.1175/JAMC-D-15-0178.1
37. Li J, Wang WC, Dong X, Mao J. Cloud-radiation-precipitation associations over the Asian monsoon region: an observational analysis. *Climate Dynam*. 2017;49(9):3237-3255. doi:10.1007/s00382-016-3509-5
38. Juan H, Da Ren L. Characteristics of solar radiation and the impact of clouds at Yangbajing, Tibet. *Atmos Ocean Sci Lett*. 2012;5(3):235-239. doi:10.1080/16742834.2012.11446994
39. Chen J, Qin X, Kang S, Du W, Sun W, Liu Y. Effects of clouds on surface melting of Laohugou glacier no. 12, western Qilian Mountains, China. *J Glaciol*. 2018;64(243):89-99. doi:10.1017/jog.2017.82
40. Hatzianastassiou N, Matsoukas C, Fotiadi A, et al. Global distribution of Earth's surface shortwave radiation budget. *Atmos Chem Phys*. 2005;5(10):2847-2867. doi:10.5194/acp-5-2847-2005
41. Liang S, Wang K, Zhang X, Wild M. Review on estimation of land surface radiation and energy budgets from ground measurement, remote sensing and model simulations. *IEEE J Sel Top Appl Earth Obs Remote Sens*. 2010;3(3):225-240. doi:10.1109/JSTARS.2010.2048556
42. Rodell M, Houser PR, Jambor U, et al. The global land data assimilation system. *Bull AAm Meteorol Soc*. 2004;85(3):381-394. doi:10.1175/bams-85-3-381
43. Slater AG. Surface solar radiation in North America: aA comparison of observations, reanalyses, satellite, and derived products. *J Hydrometeorol*. 2016;17(1):401-420. doi:10.1175/JHM-D-15-0087.1
44. Xia XA, Wang PC, Chen HB, Liang F. Analysis of downwelling surface solar radiation in China from national centers for environmental prediction reanalysis, satellite estimates, and surface observations. *J Geophys Res Atmos*. 2006;111(D9):D09103. doi:10.1029/2005JD006405
45. Gautier C, Diak G, Masse S. A simple physical model to estimate incident solar radiation at the surface from GOES satellite data. *J Appl Meteorol Climatol*. 1980;19(8):1005-1012. doi:10.1175/1520-0450(1980)019%3C1005:Aspmte%3E2.0.Co;2
46. Wu B, Liu S, Zhu W, Yan N, Xing Q, Tan S. An improved approach for estimating daily net radiation over the Heihe River bBasin. *Sensors (Basel)*. 2017;17(1):86. doi:10.3390/s17010086
47. Diak GR. Investigations of improvements to an operational GOES-satellite-data-based insolation system using pyranometer data from the U.S. cClimate rReference nNetwork (USCRN). *Remote Sens Environ*. 2017;195:79-95. doi:10.1016/j.rse.2017.04.002
48. Kim CK, Holmgren WF, Stovern M, Betterton EA. Toward improved solar irradiance forecasts: derivation of downwelling surface shortwave radiation in Arizona from satellite. *Pure Appl Geophys*. 2016;173(7):2535-2553. doi:10.1007/s00024-016-1302-3
49. Pinker RT, Laszlo I. Modeling surface solar irradiance for satellite applications on a global scale. *J Appl Meteorol Climatol*. 1992;31(2):194-211. doi:10.1175/1520-0450(1992)031%3C0194:Mssifs%3E2.0.Co;2
50. Zhang Y, Rossow WB, Lacis AA, Oinas V, Mishchenko MI. Calculation of radiative fluxes from the surface to top of atmosphere based on ISCCP and other global data sets: rRefinements of the radiative

transfer model and the input data. *J Geophys Res Atmos*. 2004; 109(D19):D19105. doi:10.1029/2003JD004457
51. Kato S, Loeb NG, Rose FG, et al. Surface irradiances consistent with CERES-derived top-of-atmosphere shortwave and longwave irradiances. *J Climate*. 2013;26(9):2719-2740. doi:10.1029/2012JD018332
52. Ma Y, Pinker RT. Modeling shortwave radiative fluxes from satellites. *J Geophys Res Atmos*. 2012;117(D23). doi:10.1029/2012JD018332
53. Wu F, Fu C. Assessment of GEWEX/SRB version 3.0 monthly global radiationdataset over China. *Meteorol Atmos Phys*. 2011;112(3):155. doi:10.1007/s00703-011-0136-x
54. Yang K, Pinker RT, Ma Y, et al. Evaluation of satellite estimates of downward shortwave radiation over the Tibetan pPlateau. *J Geophys Res Atmos*. 2008;113(D17):D17204. doi:10.1029/2007JD009736
55. Yang K, He J, Tang W, Qin J, Cheng C. On downward shortwave and longwave radiations over high altitude regions: observation and modeling in the Tibetan plateau. *Agric fFor Meteorol*. 2010;150(1):38-46. doi:10.1016/j.agrformet.2009.08.004
56. Tang W, Yang K, Qin J, Li X, Niu X. A 16-year dataset (2000-2015) of high-resolution (3 h, 10 km) global surface solar radiation. *Earth Syst Sci Data*. 2019;11(4):1905-1915. doi:10.5194/essd-11-1905-2019
57. Rao Y, Liang S, Wang D, et al. Estimating daily average surface air temperature using satellite land surface temperature and top-of-atmosphere radiation products over the Tibetan plateau. *Remote Sens Environ*. 2019;234:111462. doi:10.1016/j.rse.2019.111462
58. Hooker J, Duveiller G, Cescatti A. A global dataset of air temperature derived from satellite remote sensing and weather stations. *Scientific Data*. 2018;5(1):180246. doi:10.1038/sdata.2018.246
59. Yang Z, Yang Z, Liang F, Wang Q. Permafrost hydrological processes in Binggou Basin of Qilian Mountains (in Chinese). *J Glaciol Geocryol*. 1993;15(2):235-241.
60. Cao B, Gruber S, Zhang T, et al. Spatial variability of active layer thickness detected by ground-penetrating radar in the Qilian Mountains, Western China. *J Geophys Res Earth*. 2017;122(3):574-591. doi:10.1002/2016JF004018
61. Li X, Li X, Li Z, et al. Watershed allied telemetry experimental research. *J Geophys Res Atmos*. 2009;114(D22):D22103. doi:10.1029/2008JD011590
62. Li X, Cheng G, Liu S, et al. Heihe watershed allied telemetry experimental research (HiWATER): scientific objectives and experimental design. *Bull AAm Meteorol Soc*. 2013;94(8):1145-1160. doi:10.1175/bams-d-12-00154.1
63. Pan X, Guo X, Li X, et al. National Tibetan Plateau data center: promoting earth system science on the third pole. *Bull AAm Meteorol Soc*. 2021;102(11):E2062-E2078. doi:10.1175/bams-d-21-0004.1
64. Ran Y, Li X, Cheng G. Climate warming over the past half century has led to thermal degradation of permafrost on the Qinghai-Tibet plateau. *Cryosphere*. 2018;12(2):595-608. doi:10.5194/tc-12-595-2018
65. Yuan H, Dai Y, Xiao Z, Ji D, Shangguan W. Reprocessing the MODIS leaf area index products for land surface and climate modelling. *Remote Sens Environ*. 2011;115(5):1171-1187. doi:10.1016/j.rse.2011.01.001
66. Flerchinger G, Saxton K. Simultaneous heat and water model of a freezing snow-residue-soil system I. tTheory and development. *Trans ASABE*. 1989;32(2):565-571. doi:10.13031/2013.31040
67. Flerchinger GN, Caldwell TG, Cho J, Hardegree SP. Simultaneous hHeat and wWater (SHAW) mModel: mModel use, calibration, and validation. *Trans ASABE*. 2012;55(4):1395-1411. doi:10.13031/2013.42250
68. Yang M, Nelson FE, Shiklomanov NI, Guo D, Wan G. Permafrost degradation and its environmental effects on the Tibetan plateAUTHOR: a review of recent research. *Earth Sci Rev*. 2010;103(1):31-44. doi:10.1016/J.EARSCIREV.2010.07.002
69. Zhang Y, Cheng G, Li X, et al. Coupling of a simultaneous heat and water model with a distributed hydrological model and evaluation of the combined model in a cold region watershed. *Hydrol Process*. 2013; 27(25):3762-3776. doi:10.1002/hyp.9514
70. Dai Y, Shangguan W, Duan Q, Liu B, Fu S, Niu G. Development of a China dataset of soil hydraulic parameters using pedotransfer functions for land surface modeling. *J Hydrometeorol*. 2013;14(3):869-887. doi:10.1175/jhm-d-12-0149.1
71. Lawrence DM, Fisher RA, Koven CD, et al. The community land model version 5: description of new features, benchmarking, and impact of forcing uncertainty. *J Adv Model Earth Syst*. 2019;11(12): 4245-4287. doi:10.1029/2018MS001583
72. Burke EJ, Zhang Y, Krinner G. Evaluating permafrost physics in the coupled model Intercomparison project 6 (CMIP6) models and their sensitivity to climate change. *Cryosphere*. 2020;14(9):3155-3174. doi:10.5194/tc-14-3155-2020
73. Sándor R, Fodor N. Simulation of soil temperature dynamics with models using different concepts. *Scientific World Journal*. 2012;2012: 590287. doi:10.1100/2012/590287
74. Liu Y, Zhuang Q, Miralles D, et al. Evapotranspiration in northern Eurasia: impact of forcing uncertainties on terrestrial ecosystem model estimates. *J Geophys Res Atmos*. 2015;120(7):2647-2660. doi:10.1002/2014JD022531
75. Badgley G, Fisher JB, Jiménez C, Tu KP, Vinukollu R. On uncertainty in global terrestrial evapotranspiration estimates from choice of input forcing datasets. *J Hydrometeorol*. 2015;16(4):1449-1455. doi:10.1175/jhm-d-14-0040.1
76. Li H, Li X, Yang D, et al. Tracing snowmelt paths in an integrated hydrological model for understanding seasonal snowmelt contribution at basin scale. *J Geophys Res Atmos*. 2019;124(16):8874-8895. doi:10.1029/2019JD030760
77. Gottschalck J, Meng J, Rodell M, Houser P. Analysis of multiple precipitation products and preliminary assessment of their impact on global land data assimilation system land surface states. *J Hydrometeorol*. 2005;6(5):573-598. doi:10.1175/jhm437.1
78. Guo D, Wang H, Wang A. Sensitivity of historical simulation of the permafrost to different atmospheric forcing data sets from 1979 to 2009. *J Geophys Res Atmos*. 2017;122(22):12,269-212,284. doi:10.1002/2017JD027477
79. Saxton KE, Rawls WJ. Soil sater characteristic estimates by texture and organic matter for hydrologic solutions. *Soil Sci Soc AAm J*. 2006; 70(5):1569-1578. doi:10.2136/sssaj2005.0117

SUPPORTING INFORMATION

Additional supporting information can be found online in the Supporting Information section at the end of this article.

How to cite this article: Zhang Y, Li X, Chang X, et al. Sensitivity of simulated frozen ground temperatures to different solar radiation and air temperature products—a case study in the Qilian Mountains in West China. *Permafrost and Periglac Process*. 2023;1-17. doi:10.1002/ppp.2187

APPENDIX A

Governing equations for heat and water transfer in SHAW

In SHAW, heat and water transfer in the vertical profile from either the top of the canopy, snow or soil to a specified depth in the ground are governed by group-coupled partial differential equations on the basis of energy and mass conservation. For example, the soil heat and water transfer in SHAW is described as follows:

$$C_s\frac{\partial T}{\partial t}-\rho_i L_f\frac{\partial \theta_i}{\partial t}=\frac{\partial}{\partial z}\left[\lambda_s\frac{\partial T}{\partial t}\right]-\rho_l c_l\frac{\partial q_l T}{\partial z}-L_v\left(\frac{\partial q_v}{\partial z}-\frac{\partial \rho_v}{\partial t}\right)+E_s \quad \text{(A1)}$$

$$\frac{\partial \theta_l}{\partial t}+\frac{\rho_i}{\rho_l}\frac{\partial \theta_i}{\partial t}=\frac{\partial}{\partial z}\left[K\left(\frac{\partial \psi}{\partial z}+1\right)\right]+\frac{1}{\rho_l}\frac{\partial q_v}{\partial z}+U \quad \text{(A2)}$$

where C_s is the volumetric heat capacity of soil (J/m^3/°C); T is the soil temperature (°C); t is time (s); ρ_i is ice density (kg/m^3) and L_f is latent heat for ice fusion (335 000 J/kg); θ_i is the volumetric ice content of soil; λ_s is the thermal conductivity of soil (W/m/°C); z is the depth from the soil surface (m); ρ_l is the density of liquid soil water and c_l is its specific heat capacity (J/m/°C); q_l is the liquid water flux (kg/m^2/s); q_v is the vapor water flux (kg/m^2/s); L_v is the latent heat for water vaporization (J/kg); ρ_v is the vapor density (kg/m^3); E_s is the net energy fluxing in/out from the soil surface (W/m^2), including solar radiation, sensible heat flux, and latent heat flux; θ_l is the volumetric liquid water content of soil; K is the hydraulic conductivity of soil (m/s); ψ is the soil water potential (m); U is a source/sink term for water flux (m^3/m^3/s).

The governing equation for soil heat transfer (Equation A1) includes terms for thermal storage change, phase change of soil water, heat conduction, and heat convection caused by liquid water and vapor flux. The phase change (i.e., change in θ_i) is jointly determined by soil water content and temperature. Equation (A2) is the equation governing soil moisture transfer in the soil. Soil water transfer is mainly governed by the soil water potential (Equation A2), which is a function of soil temperature when the soil is frozen. Explicit relationships between soil potential, liquid soil water content, hydraulic conductivity, and soil temperature are necessary to solve the coupled equations, as follows:

$$\psi=\psi_e\left(\frac{\theta_l}{\theta_s}\right)^{-b} \quad \text{(A3)}$$

$$K=K_s\left(\frac{\theta_l}{\theta_s}\right)^{2b+3} \quad \text{(A4)}$$

$$\psi=\frac{L_f}{g}\left(\frac{T}{T_K}\right) \quad \text{(A5)}$$

where ψ_e is the air-entry potential of soil (m); K_s is the hydraulic conductivity of saturated soil (m/s); b is a parameter for soil pore size distribution; g is the acceleration due to gravity (9.81 m/s^2), and T_k is the absolute soil temperature (K).

For the sake of brevity, governing equations for water and heat transfer in the canopy, residue, and snow are not described here in detail, but can be found in Flerchinger and Saxton.[66] The coupled partial differential equations were solved by using the Newton–Raphson iteration technique with an implicit finite difference form in a vertically discretized system. Parameters in the equations, such as soil pore size distribution index, air-entry potential, and other hydraulic parameters, were derived by using the method described by Saxton and Rawls[79] based on the soil texture properties.